Advanced Materials

ADVANCED MATERIALS
www.advmat.de

RESEARCH ARTICLE

MOF-Functionalized Ultrasound-Trackable Magnetic Microrobots for Intracranial Toxin Removal

Yu Mei[1,2] | Shuangyi Cheng[3] | Shunyao Li[4] | Zhe Zhao[5] | Yuan Chen[1] | Jinlong Wang[1] | Guohonghao Zeng[1] | Jiayuan Huang[1] | Ji Tan[6] | Ziyu Zhang[1,2] | Guoao Ma[3] | Xuanyong Liu[5,6] | Jun Chen[4] | Kailiang Xu[3] | Xiangzhong Chen[1,2] | Yongfeng Mei[1,2] | Gaoshan Huang[1,2]

[1]International Institute for Intelligent Nanorobots and Nanosystems, College of Intelligent Robotics and Advanced Manufacturing, State Key Laboratory of Surface Physics, and State Key Laboratory of Photovoltaic Science and Technology, Fudan University, Shanghai, P. R. China | [2]Zhejiang Key Laboratory of Extreme Environment Functional Materials, Yiwu Research Institute of Fudan University, Yiwu, P. R. China | [3]College of Biomedical Engineering, Fudan University, Shanghai, P. R. China | [4]Sports Medicine Institute of Fudan University, Department of Sports Medicine, Huashan Hospital, Fudan University, Shanghai, P. R. China | [5]College of Biological Science and Medical Engineering, Donghua University, Shanghai, P. R. China | [6]State Key Laboratory of High Performance Ceramics, Shanghai Institute of Ceramics, Chinese Academy of Sciences, Shanghai, P. R. China

Correspondence: Zhe Zhao (zhezhao@dhu.edu.cn) | Kailiang Xu (xukl@fudan.edu.cn) | Xiangzhong Chen (xzchen@fudan.edu.cn) | Yongfeng Mei (yfm@fudan.edu.cn) | Gaoshan Huang (gshuang@fudan.edu.cn)

Received: 21 August 2025 | **Revised:** 16 November 2025 | **Accepted:** 12 December 2025

Keywords: detoxification | magnetic navigation | metal–organic framework | microrobot | ultrafast ultrasound imaging

ABSTRACT

Toxin accumulation within specialized microenvironments, such as cerebrospinal fluid (CSF), poses significant clinical challenges. In particular, bilirubin in CSF can cause severe damage to the brain and neural tissues. Current therapeutic strategies for intracranial bilirubin clearance suffer from poor targeting, inadequate detoxification capacity, and reliance on invasive procedures. Here, we demonstrate multifunctional microrobots designed for toxin removal in specialized anatomical compartments. The proposed ultrasound-trackable microbubbles@PCN-333 microrobots (UMPCs) feature a hollow hydrogel microbubble core for enhanced ultrasound imaging contrast, an outer metal–organic framework (MOF) layer for proactive and high-capacity toxin adsorption, and embedded ferroferric oxide (Fe_3O_4) nanoparticles to enablec. Magnetic actuation enhances the UMPC's bilirubin capture efficiency through improved mass transfer. By integrating an ultrafast ultrasound imaging system with magnetic actuation, we achieve real-time tracking and precise control of UMPCs within the CSF. This strategy offers a minimally invasive and actively guided approach for efficient intracranial bilirubin clearance, opening new avenues for targeted toxin-removal in anatomically confined environments.

1 | Introduction

The pathological accumulation of neurotoxic metabolites within anatomically protected compartments—such as the cerebrospinal fluid (CSF), synovial cavities, vitreous body, and urinary bladder—can trigger severe and irreversible damage [1–4]. Among them, the central nervous system in CSF is particularly vulnerable due to its delicate nature and limited regenerative capacity, despite protection by the blood-brain barrier and blood-CSF barrier [5, 6]. For instance, bilirubin-induced neurotoxicity can lead to acute bilirubin encephalopathy (ABE), characterized by irreversible neuronal damage through

Yu Mei and Shuangyi Cheng contributed equally to this work.

multiple mechanisms, including mitochondrial dysfunction, synaptic impairment, and neuroinflammation [7–9]. However, current clinical interventions can only rely on invasive procedures with limited efficacy and fail to target toxins deep within the closed compartments [10, 11].

Extracorporeal circulation and adsorption provide a less-invasive alternative for detoxification. Metal–organic frameworks (MOFs), such as PCN-333 (Fe), have emerged as a group of promising candidates to increase the adsorption efficiency [12–14] due to their high surface area and thus exceptional affinity to toxins such as bilirubin [15]. However, this approach relies on passive adsorption, remaining inadequate for rapid and targeted toxin removal in vivo [11, 16]. Recently developed medical microrobots offer a paradigm-shifting alternative, with demonstrated capabilities of localized therapy, such as drug delivery in the bladder, intracranial tumor management, endovascular thrombolysis, and intra-articular biofilm eradication [17–29]. MOF-based microrobots combine the high porosity with controlled locomotion [12–14], making them promising candidates for active in vivo detoxification. Nevertheless, challenges persist, including limited control of locomotion in confined spaces and lack of deep-tissue real-time monitoring with sufficient spatiotemporal resolution, biosafety, and clinical practicality [30–32].

Here, we introduce a multifunctional microrobotic system: ultrasound-trackable microbubbles@PCN-333 (Fe) (UMPCs), featuring a gas-core hydrogel microbubble for ultrasound contrast, an outer MOF shell for active bilirubin adsorption, and embedded superparamagnetic iron oxide nanoparticles for magnetically controlled locomotion. Magnetic actuation enhances bilirubin removal efficiency through active fluid mixing and improved mass transfer. The integrated design enables precise and real-time tracking, targeting, and detoxification. We validate this approach through in vitro bilirubin adsorption tests and in vivo intracranial experiments in rabbits. This strategy offers a transformative solution not only for bilirubin removal in CSF, but also for microrobot-assisted detoxification in other specialized physiological environments.

2 | Results and Discussion

2.1 | System Design

Figure 1 illustrates the design concept of the microrobotic platform. We first generated nitrogen-core microbubbles by using a microfluidic chip. Then, we employed atomic layer deposition (ALD) to grow a zinc oxide (ZnO) nanomembrane on the surface of the microbubble, which serves as a seed layer for the subsequent growth of PCN-333 (Fe) MOF layer. Magnetic nanoparticles, i.e., ferroferric oxide (Fe_3O_4) nanoparticles, were then incorporated to render these UMPCs magnetically responsive, allowing enhanced mass transfer under external magnetic fields, and thereby improved detoxification efficiency (Figure 1a). The resulting UMPCs can be precisely navigated within the CSF using a magnetic control system and simultaneously monitored via high-speed ultrasound imaging at a processing speed of over 10 000 frames per second (Figure 1b; Table S1). This enables real-time tracking and localization with high spatiotemporal resolution (left image of Figure 1b(i)). Spectra in the right part of Figure 1b(ii) experimentally confirm the removal of bilirubin by UMPCs, as the absorption from residual bilirubin decreases gradually with time.

2.2 | Fabrication and Characterization of UMPCs

The UMPC incorporates a gas-core hydrogel bubble fabricated via microfluidic technology to enhance ultrasound contrast (Figure 2a) [33]. Two tapered capillaries were aligned coaxially within an encapsulating square tube, allowing the simultaneous introduction of three fluid phases: nitrogen (inner phase), 4 wt.% polyvinyl alcohol (PVA) solution (middle phase), and a hydrogel precursor solution composed of methacrylic anhydride (MAAn), ethylene glycol dimethacrylate (EGDMA), and 2-hydroxy-2-methylpropiophenone (outer phase). The shear stress exerted by the continuous outer stream breaks the inner gas stream at the outlet (Figure S1 and Video S1), resulting in the formation of microbubbles that are rapidly cured by UV light.

We first evaluated how the shell thickness-to-core radius ratio affects mechanical deformation and ultrasound imaging performance of microbubbles. On the one hand, as the ratio increases, the internal stress within the shell of the microbubble decreases under an applied 1 MPa local pressure (Figure 2b; Figure S2), but when the ratio is over 0.1, the strain in the shell does not change much (Figure S2). On the other hand, the smaller the ratio is, the better the ultrasound imaging performance of the microbubble is (Figure S3). Guided by the simulation results, we then selected an optimal ratio of ~0.1 based on tradeoff and prepared the microbubbles (Figure 2c; Figure S4). In addition, the mechanical stability of the UMPCs in body fluid should be evaluated. In our work, we simulated internal stress distribution within the shell of microbubble in a liquid environment with global compression pressure applied (Figure S5), and the results indicate good mechanical stability of the microbubble in body fluid, where no damage can be produced due to relatively small strain in the shell. Corresponding experiment were carried out in artificial CSF (aCSF) with UMPCs immersed, and a global compression pressure of 2 kPa was applied ten times to simulate intracranial pressure (Figure S6). The intactness of the UMPCs after the process is noticeable, demonstrating that the mechanical stability of the UMPCs fully meets the requirements of practical biomedical applications. Moreover, the size of the hydrogel microbubbles can be precisely tuned from 10 to 200 μm by adjusting the flow rates of the outer and middle phases (Figure 2d; Figure S7). Figure 2e(i),(ii) are scanning electron microscopy (SEM) image and optical microscopy image of a microbubble, respectively, and the shell structure can be clearly observed from a broken microbubble shown in Figure S8a. This shell can then be precisely visualized by 3D optical coherence tomography (Figure S8b).

Then, hydrogel microbubbles were coated with a ZnO nanomembrane deposited by using ALD (named as microbubble@ZnO, see Figure S8c) followed by hydrothermal growth of PCN-333 (Fe) (named as microbubble@PCN-333 (Fe), see Figure 2e(iii),(iv); Figure S8d). Figure S8d also demonstrates that a gas core remained intact in a microbubble after these fabrication steps, and we experimentally confirmed that only ~9% of the microbub-

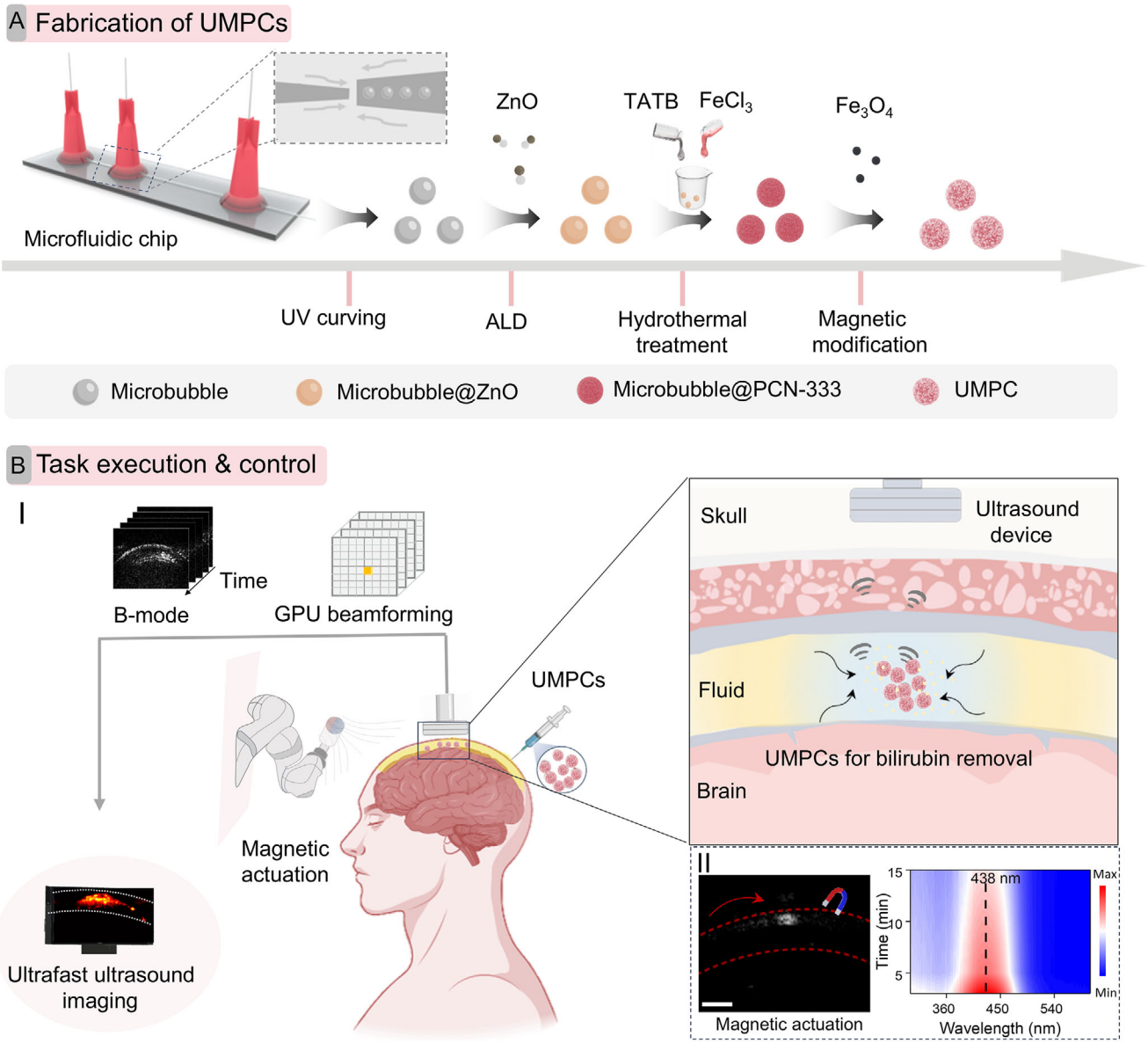

FIGURE 1 | Fabrication and medical task of UMPCs. (A) Schematic of the fabrication process. (B) Schematic of intracranial detoxification of UMPCs under magnetic actuation and ultrafast ultrasound imaging (Panel (i)). Panel (i) is adapted from figure created in BioRender. Mei, Y. (2025) https://BioRender.com/os1knki. Panel (ii) in (B) is ultrasound image of UMPCs obtained in a brain model (left) and absorption spectra of residual bilirubin in PBS confirming the adsorption process (right).

bles were damaged during hydrothermal growth, indicating a good stability. The energy dispersive X-ray (EDX) spectrometry characterizations of the samples after magnetic modification, i.e., UMPCs, in Figure 2f and Figure S9 show that Fe, C, N, and O elements exist in UMPCs and are uniformly distributed. The N content is twice as high as that of Fe, implying the successful assembly of the PCN-333 (Fe) layer. It is worth noting that the ZnO nanomembrane prepared by ALD is crucial for the growth of a uniform MOF layer on the surface with high loading (Figure S10) [34, 35], as the ZnO nanomembrane acts as a nucleation layer for the formation of Zn,Fe-hydroxy double salt (HDS), which ultimately transforms to PCN-333 (Fe) (Figure S11) [36]. UMPCs with MOF layers of three different thicknesses were prepared in the experiments: UMPC-1 (thick layer, Figure S12a), UMPC-2 (middle layer, Figure S12b), and UMPC-3 (thin layer, Figure S12c). Here, the thickness of ZnO nanomembrane is linearly proportion to the number of ALD cycles (Figure S13), and we also found a positive correlation between the thickness of the ZnO nanomembrane and the quality of the formed PCN-333 (Fe) layer [37]. Namely, increasing ZnO nanomembrane thickness improves MOF layer quantity and uniformity as well as the content of PCN-333 (Fe). In this work, we studied the influence of ZnO nanomembrane thickness on the MOF layer. As illustrated in Figure S14, the thermogravimetric analysis (TGA) of different samples proves that UMPC-1 possesses the highest amount of PCN-333 (Fe), while the PCN-333 (Fe) loading in UMPC-3 is the lowest. The approach also enables the growth of PCN-333 (Fe) layers on microbubbles with different diameters ranging from ~20 to 300 μm (Figure S15), demonstrating its universal applicability.

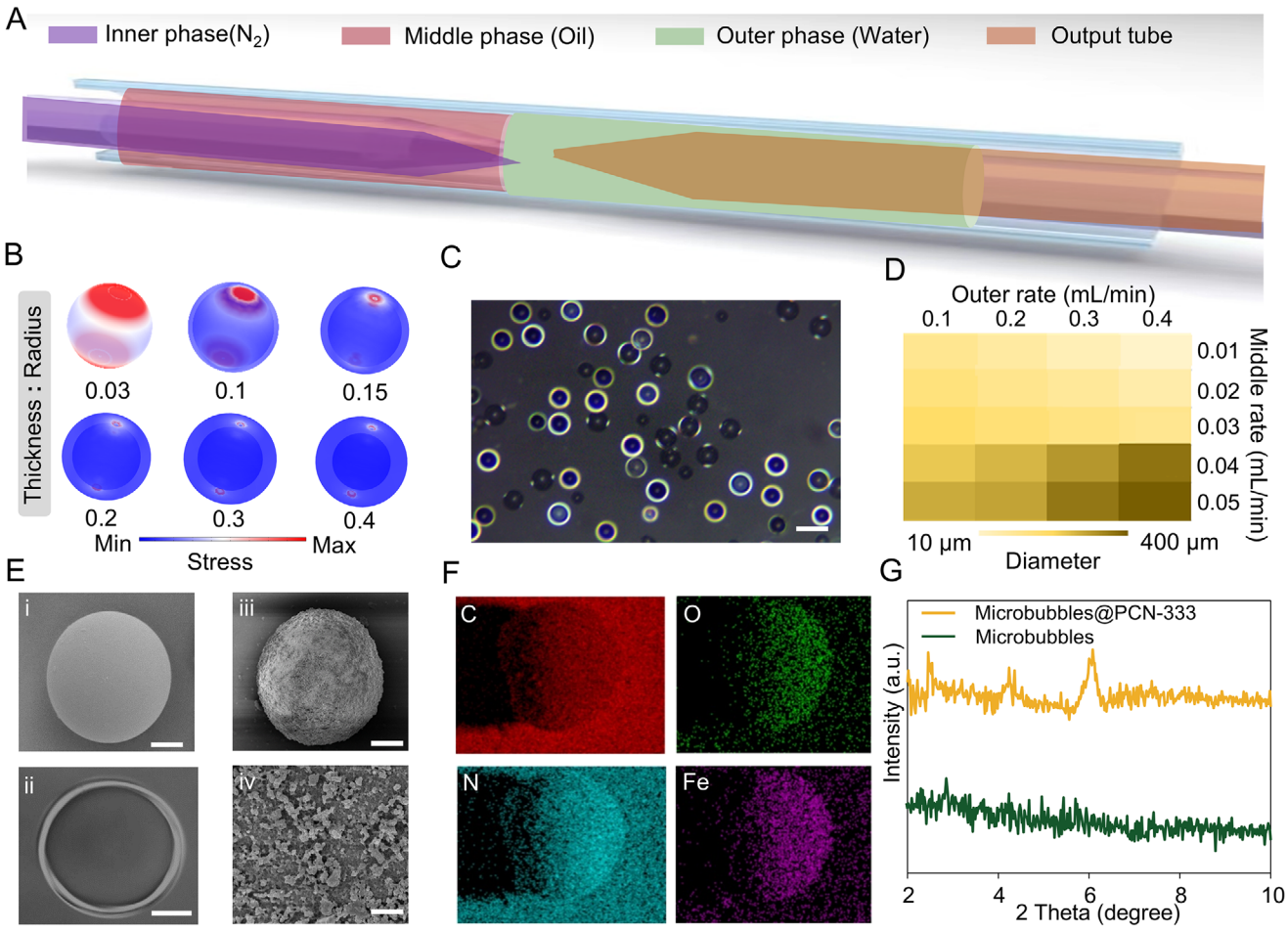

FIGURE 2 | Fabrication and characterization of microbubble and UMPCs. (A) Schematic diagram of the configuration of the microfluidic chip. (B) Simulated deformation of microbubble with different shell thicknesses under a local stress of 1 MPa in an area of approximately 18.7 μm^2. (C) An optical microscopy image of hydrogel microbubbles. (D) Tuning of microbubble diameter by altering the flow speed of the middle phase and outer phase. (E) SEM image (i) and an optical microscopy image (ii) of a microbubble, SEM image (iii) of a UMPC, and a magnified SEM image (iv) of the surface of a UMPC. Scale bars are 20 μm for panels (i–iii) and 500 nm for panel (iv). (F) EDX mapping of C, O, N, and Fe of the UMPC in (e(iii)). (G) XRD patterns of microbubbles and microbubbles@PCN-333 (Fe).

The X-ray diffraction (XRD) pattern of microbubbles@PCN-333 (Fe) is shown in Figure 2g, which matches that of PCN-333 (Fe) [36], confirming the crystalline nature of the grown PCN-333 (Fe) layer. The absorption bands at 1651 and 1400 cm^{-1} in Fourier transform infrared (FTIR) spectrum of microbubbles@PCN-333 (Fe) in Figure S16 represent the stretching of -COOH, indicating the existence of dicarboxylates coordinated with metal ions [38]. The peaks at 702 cm^{-1} are characteristic of skeleton vibration of aromatic heterocycles and triazine nuclei, indicating the presence of 2,4,6-Tris(4-carboxyphenyl)-1,3,5-triazine (H_3TATB) connectors [39]. Additionally, the peak at 517 cm^{-1} corresponds to the stretching mode of Fe-O [40]. X-ray photoelectron spectrum (XPS) of UMPCs in Figure S17 confirms the presence of Fe, O, and C, and the peak of Fe 2p in the high-resolution spectra can be deconvoluted into three peaks at 725.3, 711.4, and 715.7 eV, corresponding to Fe $2p_{1/2}$, Fe $2p_{3/2}$, and satellite species peaks, respectively [41]. The Brunauer–Emmett–Teller (BET) measurements (Figure S18) demonstrate an increase in the surface area from 0.75 m^2/g for hydrogel microbubbles to 43 m^2/g for UMPCs, due to the presence of the porous structure in the PCN-333 (Fe) layer (inset of Figure S18).

2.3 | Magnetically Controlled Locomotion of UMPCs

The magnetic properties of UMPCs arise from embedded Fe_3O_4 nanoparticles, as confirmed by the hysteresis loop in Figure S19. These nanoparticles make UMPCs highly sensitive to external magnetic fields (Figure S20), enabling precise motion control of UMPCs. We first examined the motion behavior of a single UMPC under rotating magnetic fields. Two different motion modes were observed: fixed spinning and rolling (Figure 3a). As detailed in Note S1, the motion is governed by magnetic force (F_m) and magnetic torque (T_m). When the pitch angle of the input magnetic field is 0° with respect to z-axis (i.e., an in-plane rotating field), the UMPC rotates in place (fixed spinning mode). At non-zero pitch angles, the UMPC rolls directionally (rolling mode). Rolling modes with pitch angles of 45° and 90° with respect to z-axis are schematically shown in Figure 3a, and pitch angle of ~45° was commonly used in our experiment for magnetic navigation. In addition, the motion of the UMPCs was also investigated in various biological fluids (Figure 3b; Figure S21) to evaluate the wide applicability of the UMPCs

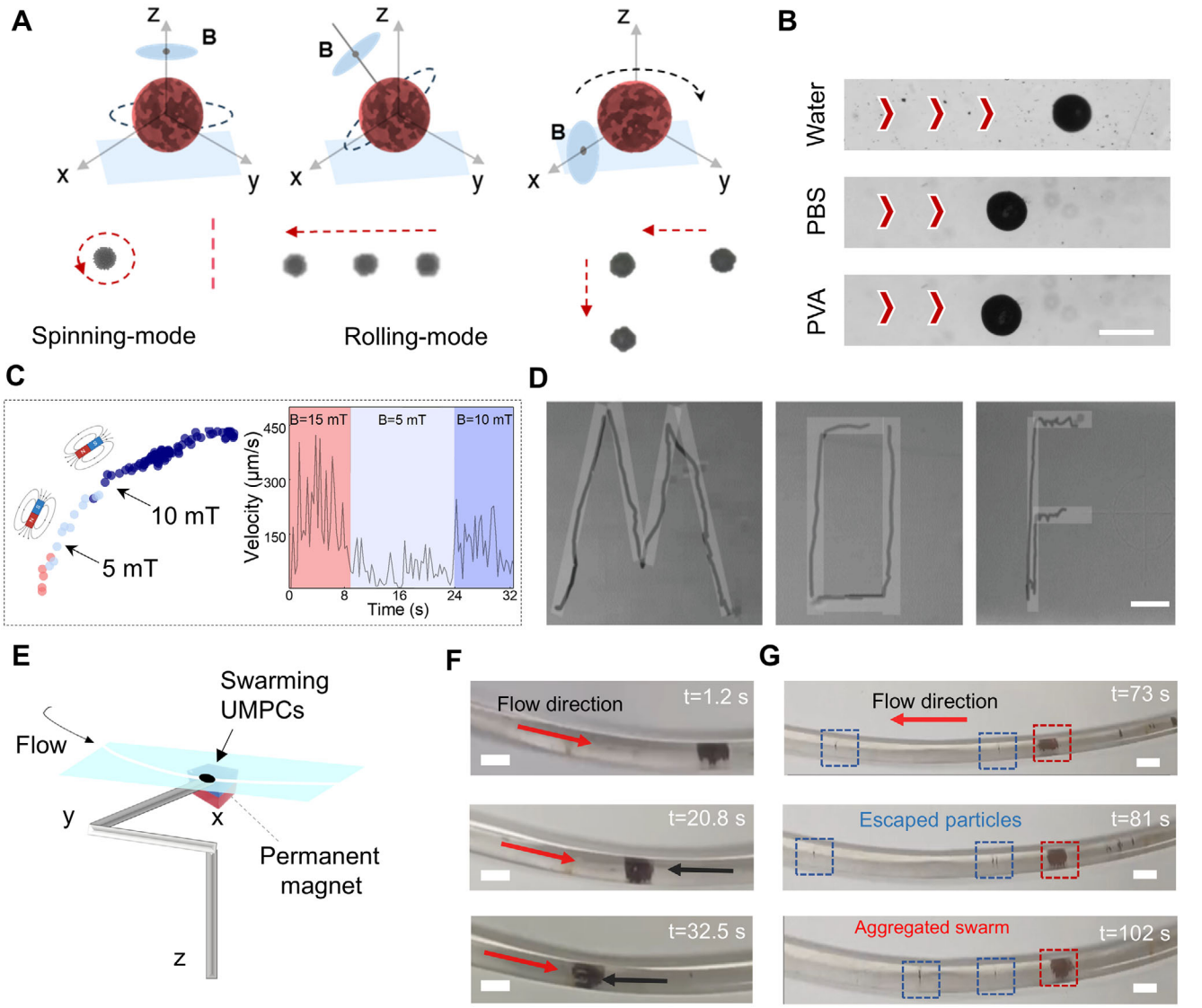

FIGURE 3 | Magnetic field-controlled locomotion of UMPCs. (A) Schematic of two different motion modes in a rotating magnetic field: fixed spinning and rolling. (B) Navigability of UMPCs in various media under a rotating magnetic field (5 mT, 5 Hz). Scale bar: 100 μm. (C) Trajectory and velocity variation of a single UMPC under varying field strengths. (D) Path-following motion of a UMPC along "M", "O", and "F" trajectories. The rotating magnetic field used is 10 mT, 5 Hz. Scale bar: 1 mm. (E) Schematic of the magnetic manipulation setup. (F) Images showing a swarm of UMPC swimming upstream in a body fluid environment under an external magnetic field. (G) Images showing aggregated versus escaped UMPCs. Scale bars in (F) and (G) are 2 mm.

in various environment for advantageous bio-applications, and effective movement and navigation in water, phosphate buffer saline (PBS), 5% PVA, and PBS containing 10 % fetal bovine serum (FBS) and 1% bovine serum albumin (BSA) under rotating magnetic field were observed. As illustrated in Figure 3c, motion speed ranging from ~50 μm·s^{-1} at 5 mT to ~300 μm·s^{-1} at 15 mT was realized, and the speed tunability is also evidenced by Video S2. The field-responsive behavior allows precise directional control and path programming, as demonstrated by, e.g., "M", "O", and "F" trajectories with small deviation (Figure 3d). The UMPC's ability to navigate complex intracranial anatomical structures was further confirmed in a 3D-printed resin brain sulcus-mimicking model filled with aCSF, where UMPCs move effectively and smoothly under a magnetic field of 10 mT (Figure S22).

In a more realistic fluid environment, collective motion of UMPCs can also be achieved. Here, we modeled the body fluid environment by using 5% PVA or aCSF with circulating flow (Figure 3e). A magnetic manipulation system consisting of a spherical permanent magnet and a robotic arm were used to provide a stronger magnetic field of 20 mT, which can concentrate the swarming UMPCs in the fluid (Figure S23), and even produce an upstream motion over time (Figure 3f; Figure S24 and Video S3). More, maintaining the swarm cohesion is crucial for practical applications, as the escaped UMPCs could reduce the treatment efficacy. Figure 3g and Figure S25 demonstrate that the escape rate under a 20 mT magnetic field is only ~9% within 3 min. Considering the 3D geometry of the swarm, the actual escape rate could be even lower. These compelling results indicate that the swarming UMPCs can effectively respond to magnetic fields

within complex internal environments, which is crucial for in vivo applications.

2.4 | Ultrafast Ultrasound-Guided Navigation of UMPCs In Vitro

The gas core of the UMPCs enhances the echo of ultrasound, enabling their detection via ultrafast ultrasound imaging (Figure 4a). As shown in the lower panel of Figure 4a and Figure S26, we compared the ultrasound signals of UMPCs, solid hydrogel microspheres (HMs), and a blank control (water). The UMPCs exhibited echo intensities approximately four times higher than those of HMs (Figure 4b; Video S4). Acoustic numerical simulations (Figure 4c,d) in both time and frequency domains further confirm that the echo signal of UMPCs with a shell thickness-to-core radius ratio of 1:10 is approximately three times higher than that of HMs, facilitating efficient tracking via ultrasound imaging (Note S2).

To evaluate imaging performance at different anatomical depths, we simulated B-mode ultrasound images of UMPCs at different depths ranging from 8 to 40 mm. Signal attenuation is observed with increasing depth; however, UMPCs remain clearly visible at 40 mm while the HMs become hardly detectable (Figure 4e). For quantitative analysis, the contrast-to-tissue ratio (CTR) for both HMs and UMPCs at different depths was calculated (Figure S27), and the obtained CTRs are presented in Table S2. This quantitative analysis suggests that UMPCs are well-suited for in vivo deep-tissue imaging with ultrasound. Moreover, under a magnetic field of 10 mT, 5 Hz, UMPCs demonstrated rapid responsiveness and aggregated within 10 s, as evidenced by ultrasound imaging (Figure 4f). This fast behavior enables precise manipulation and efficient post-deployment collection and reuse, which highlights their potential for biomedical applications, especially in dynamic and complex fluidic environments [42]. To mimic physiological navigation, UMPCs were guided along predefined trajectories within a complex microchannel network under a rotating magnetic field (20 mT, 5 Hz). The results shown in Figure 4g and Video S5 and the extracted image in Figure S28 showcase UMPC's ability to navigate in complex intracranial flows and intricate spatial environments with high precision for targeted therapeutic applications and localized detoxification.

For directional visualization of UMPCs within the fluidic channels, ultrafast Doppler ultrasound imaging was employed. The Doppler shift in color Doppler (CD) mode enabled real-time differentiation of vertical motion [43], with blue and orange indicating upward and downward motions, respectively (Figure 4h; Figures S29 and S30). In the experiment, sheep erythrocytes were introduced to simulate in vivo blood flow, which flowed from top to bottom driven by a pump, thus appearing to be blue; whereas the UMPCs were moving upward against the blood flow under magnetic guidance (20 mT, 5 Hz), thus appearing to be orange. This highlights the system's capacity to detect and differentiate microrobot motion in a real-time manner, an essential feature for in vivo applications. Additionally, the speed of the swarming UMPCs was quantitatively analyzed by using Doppler techniques. As demonstrated in Figure S30, the bulk flow velocity is determined to be ~1 mm·s^{-1}, while the UMPCs swarm moves at a velocity of ~−0.2 mm·s^{-1} in a rotating magnetic field (20 mT, 5 Hz), signifying motion against the prevailing fluid flow. This quantitative assessment validates the accuracy and reliability of this imaging system in measuring the speed of UMPCs within dynamic environments. Such precise measurements are critical for understanding the interaction between microrobots and the surrounding medium, providing insights into their behavior under physiological flow conditions.

2.5 | Bilirubin Adsorption and In Vitro Detoxification by UMPCs

Figure 5a illustrates that while actuated with external magnetic field, UMPCs are capable of effectively adsorb bilirubin with PCN-333 (Fe) layer. To evaluate adsorption performance, an initial bilirubin concentration of 120 mg·L^{-1}, which is known to cause organ damage was selected [15]. The evolutions of bilirubin concentration as a function of adsorption time for UMPCs with different amounts of PCN-333 (Fe) are shown in Figure 5b. The results indicate that all three samples achieve adsorption equilibrium within 10 min, reducing bilirubin concentrations to 8.2 (UMPC-1), 36.1 (UMPC-2), and 99.2 (UMPC-3) mg·L^{-1}. Notably, the UMPC-1 reduces bilirubin levels to below the normal threshold (<12.5 mg·L^{-1}). In contrast, hydrogel microbubbles without MOF coatings show limited adsorption of bilirubin (Figure S31). To investigate the adsorption mechanism, kinetic data were fitted using pseudo-first-order and pseudo-second-order models [44], and the results are presented in Figure 5c and Figure S32, Note S3, and Tables S3 and S4. Based on the correlation coefficient (R^2), the data fit the pseudo-second-order model best, indicating that the adsorption process is primarily governed by chemical interactions [15], and the adsorption rate is dependent on both the availability of active sites and the concentration of bilirubin molecules in the vicinity of these sites [45]. The pseudo-second-order model further supports the hypothesis that the adsorption mechanism involves the stable complex formation between bilirubin and the PCN-333 (Fe), with the rate-limiting step being the chemical binding rather than diffusion [46]. Subsequently, we estimated the maximum adsorption capacity and adsorption isotherm of the UMPC-1 by utilizing Langmuir and Freundlich models [47]. The Langmuir model, which assumes monolayer adsorption on uniform active sites, exhibits a better fitting, indicating homogeneous adsorption behavior. The maximum adsorption capacity deduced from the Langmuir model is found to be 48.96 mg·g^{-1} (Figure 5d).

To simulate the interference of various proteins with toxin clearance processes under realistic physiological conditions, competitive adsorption was studied in the presence of 40 mg·mL^{-1} BSA, as shown in Figure 5e. Absorption spectra in Figure S33 show that the absorption peak of bilirubin bound to BSA is at 460 nm, and UMPC removed 72.3% of bilirubin after 30 min treatment, while the BSA concentration remained nearly unchanged (Figure 5e). This selectivity is attributed to the size exclusion effect, as the pore size of PCN-333 (Fe) is significantly smaller than the size of BSA [15]. Density functional theory (DFT) calculations (Figure S34 and Note S4) further confirm this phenomenon by showing an adsorption energy of 1.47 eV for bilirubin on PCN-333 (Fe), which is substantially higher than that of several other representative adsorbents, indicating a strong interaction and corresponding selectivity.

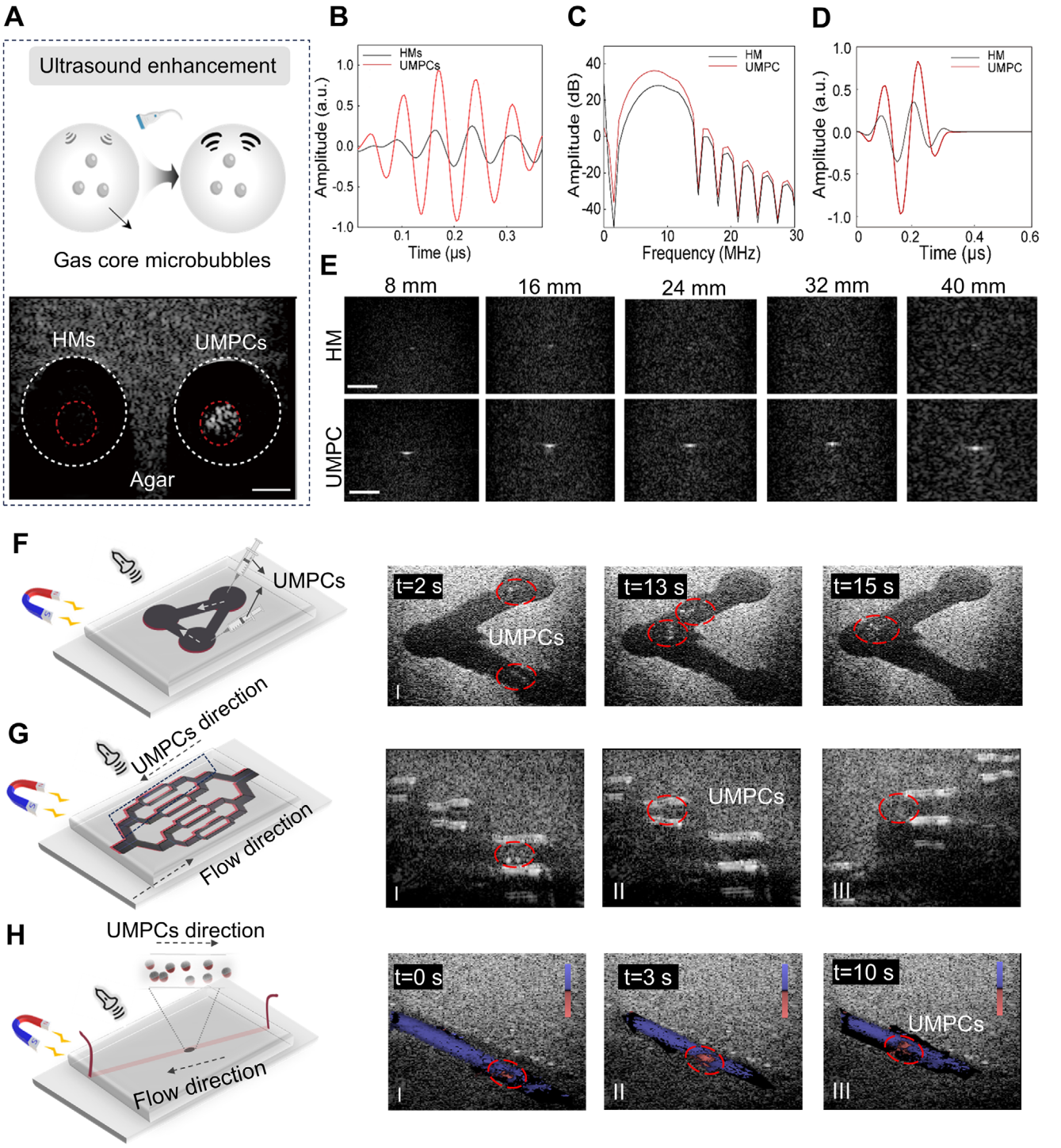

FIGURE 4 | In vitro ultrasound imaging and tracking of UMPCs. (A) Schematic illustration of enhanced ultrasound reflectance from gas-core microbubble (upper panel) and ultrasound images of UMPCs and solid HMs in an agar phantom (lower panel). Scale bar: 5 mm. (B) Experimental time-domain ultrasound signal of UMPCs compared with solid HMs. Simulated ultrasound reflectance spectra of UMPCs and HMs in (C) frequency domains and (D) time domain. (E) Simulated B-mode ultrasound images of UMPCs and HMs at different depths. Scale bar: 2 mm. (F,G) B-mode ultrasound images showing magnetic field-induced aggregation and navigation of UMPCs moving in structured microchannels filled with PBS. (H) Doppler ultrasound images illustrating directional upstream motion of UMPC swarm in sheep blood flow under magnetic field guidance. Flow rates in G and H are 2 mL min^{-1}, and the magnetic field strengths used in (F–H) are 10, 20, and 20 mT, respectively.

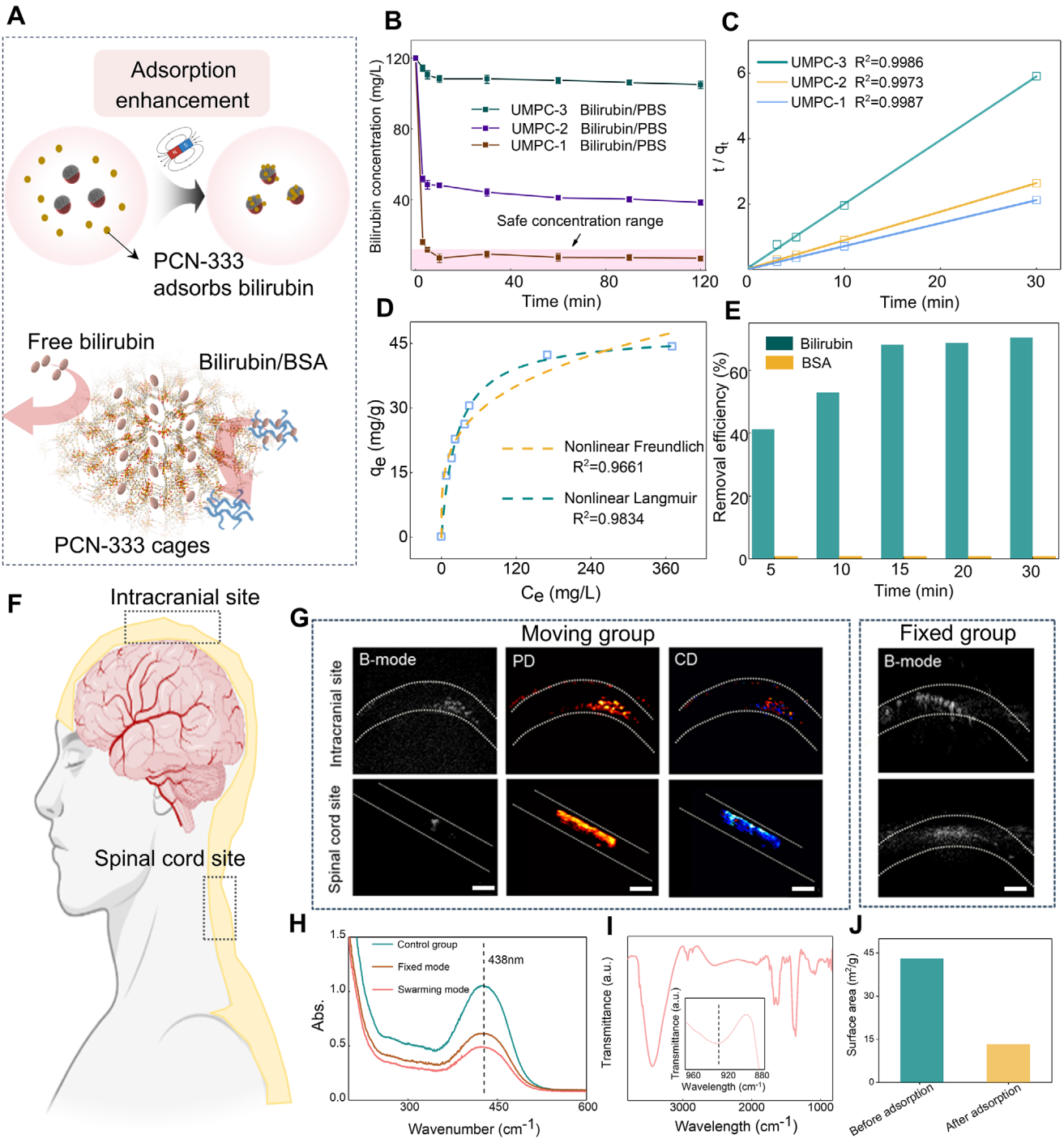

FIGURE 5 | Adsorption of UMPCs toward Bilirubin in vitro. (A) Schematic illustration of the adsorption process for bilirubin. (B) Bilirubin concentration as a function of adsorption time in PBS. The initial bilirubin concentration is 120 mg·L^{-1}. UMPCs with different amounts of PCN-333 (Fe) are used ($n = 3$, data are presented as the mean ± standard deviation). (C) Kinetic fitting of bilirubin adsorption using pseudo-second-order model. Open squares represent experimental data. (D) Bilirubin adsorption isotherms of UMPC-1. The open squares are experimental data, and the dashed lines are corresponding fitting curves. (E) Removal efficiency for bilirubin/BSA. The initial BSA concentration is 40 mg·mL^{-1} and the initial bilirubin concentration is 120 mg·L^{-1}. (F) Schematic of UMPCs performing detoxification in CSF at different locations. Adapted from figure created in BioRender. Mei, Y. (2025) https://BioRender.com/os1knki. (G) B-mode, PD mode, and CD mode ultrasound images of UMPCs under different motion modes in various regions filled with PBS. (H) The UV-visible absorption spectra of corresponding liquid samples. (I) The FTIR spectrum of UMPCs after bilirubin capture. The inset shows the new absorption band assigned to the captured bilirubin. (J) The surface area of UMPCs before and after bilirubin capture.

To demonstrate the dynamic adsorption of bilirubin by UMPCs in CSF, we developed an in vitro circulation model using a gelatin brain phantom and a 3 mm-diameter tube connected to a circulation pump (Figure S35), with a flow rate of ~0.3 $cm \cdot s^{-1}$ [42]. Figure 5f shows the schematic of UMPCs performing detoxification in CSF at the intracranial site and spinal cord site. Experimentally, UMPCs were deployed into the tube with the assistance of a catheter and monitored in real time using ultrasound imaging at various locations. B-mode, power Doppler (PD), and CD modes were used to probe both motion and directionality details of the UMPCs under the magnetic actuation (Figure 5g). Comparison between moving UMPCs (controlled by time-varying magnetic field) and fixed UMPCs (fixed with a stationary permanent magnet) shows significantly greater bilirubin removal after 10 min for the moving group, as confirmed by the UV–vis absorption spectra in Figure 5h. Computational fluid dynamics simulations (Figure S36) revealed that the rotation of UMPCs under magnetic fields produces localized disturbance, enhancing mass transfer by disrupting the fluid's flow and inducing turbulence, and this active mixing facilitates faster transport of bilirubin molecules toward the surface of UMPCs. A new peak at 925 cm^{-1} appears in the FTIR spectrum of UMPCs after the capture experiment, indicating the presence of bilirubin on UMPCs' surface, further confirming the efficient adsorption (Figure 5i). In addition, we found an obvious decrease of the specific surface area from 43 to 13.2 m^2/g for UMPCs after bilirubin capture (Figure 5j), indicating the surface coverage by adsorbed molecules. Since the stability of the PCN-333 (Fe) layer in CSF is crucial for its continuous functionality, we check the structural property of UMPC after a 72-h immersion in aCSF, and the obtained XRD pattern (Figure S37) proves that the PCN-333 (Fe) layer attaches firmly on the surface of UMPC and its crystal structure remains unchanged after such a long immersion time. Collectively, these results demonstrate that UMPCs can perform efficient and selective bilirubin removal in a circulating and confined fluid environment. Their activity can be dynamically controlled and monitored in real time by using ultrafast ultrasound imaging, offering strong potential for in vivo detoxification applications.

2.6 | In Vivo Validation of UMPCs Navigation and Biosafety

Building on the in vitro results, we conducted in vivo experiments to assess the clinical applicability of UMPCs in a rabbit model (Figure 6a,b). The entire surgical procedure is detailed in Figure S38a, where a craniotomy is performed under real-time ultrasound monitoring—a common method in neurosurgical diagnostics and the implantation of metallic instruments. The UMPCs were precisely injected into CSF within the subarachnoid space via a catheter. Then the UMPCs are driven by an external magnetic field (20 mT, 2 Hz) within the CSF between the brain tissue and meninges, and monitored real-time by ultrasound imaging (Video S6). Figure 6c demonstrates the magnetic field intensity distribution of the actuation magnetic field in the xy-plane. Swarm 1 reached the imaging plane at t = 0 s, resulting in a peak signal intensity that gradually faded as it exited the plane. Conversely, Swarm 2 entered at t = 3.94 s, producing an increasing signal over time (Figure 6d). These results confirm that UMPCs can be precisely manipulated and monitored in vivo, even within the constrained volume of the cranial cavity. After a period of ~10 min, a customized biocompatible neodymium-iron-boron (NdFeB) magnetic needle was used to retrieve the UMPCs (Figure S38b). Figure 6e and Figure S39 demonstrate that this needle can effectively collect the UMPCs from the cranial cavity without damaging the cerebral vasculature. Experimental and simulation results confirmed that the UMPCs experienced magnetic force from the needle's field (Figure S39a,b). No signs of hemorrhage were observed after 1 cm insertion, and the titanium (Ti) coating on the needle ensures biocompatibility and minimized bacterial infection risk (Figure S39c).

Post-operative observations (Figure S40) indicated a slight transient weight loss following catheter implantation, which gradually recovered within a few days. No statistically significant differences were observed among the UMPCs-treated rabbit, craniotomy-treated rabbit, and control, and no adverse neurological effects, such as limb paralysis or motor dysfunction, were observed in any of the rabbits during the study. Overall, the experimental results indicate that intracranial treatment with UMPCs had minimal impact on the health of the rabbits, with the primary injury arising from the craniotomy procedure. After the experiment, the animals were euthanized for histological analysis. Hematoxylin and eosin (H&E) staining revealed no pathological changes in brain tissue or major organs in any of the experimental groups, with no signs of edema, degeneration, or inflammatory infiltration (Figure S41), and cytotoxicity experiments confirmed low cytotoxicity of UMPCs toward vascular endothelial cells (Figure S42). In addition, experimental results confirmed that UMPCs treatment did not significantly alter the levels of inflammatory cytokines throughout the body (Figure 6f). Blood-brain barrier (BBB) integrity was assessed by Evans blue extravasation. The middle cerebral artery occlusion (MCAO) model served as a positive control, confirming the expected BBB disruption with significant dye leakage. In contrast, both UMPCs-treated and control (healthy) groups, which did not undergo MCAO, showed minimal and comparable levels of leakage (Figure 6g; Figure S43). This result demonstrates that UMPCs treatment itself does not compromise BBB integrity. In addition, Prussian blue staining performed on brain sections at 7 and 14 days after UMPCs treatment reveals no evident iron deposition, comparable to the control group (Figure 6h). In order to evaluate the potential impact of UMPCs on cerebral oxidative stress levels, the content of malondialdehyde (MDA), a marker of lipid peroxidation, and the activity of superoxide dismutase (SOD), a key antioxidant enzyme, were measured at 7 and 14 days after the treatment. No significant differences in cerebral MDA or SOD were found among the groups (Figure S44), suggesting that UMPCs administration did not elicit a significant oxidative stress response in the brain. These findings support the feasibility, safety, and controllability of UMPCs in a live intracranial environment, laying the foundation for transitioning UMPCs to surgical applications.

3 | Conclusions

In this study, we developed a microrobotic platform (i.e., UMPC) fabricated via a combination of microfluidics fabrication and ALD-assisted hydrothermal synthesis. This approach enables

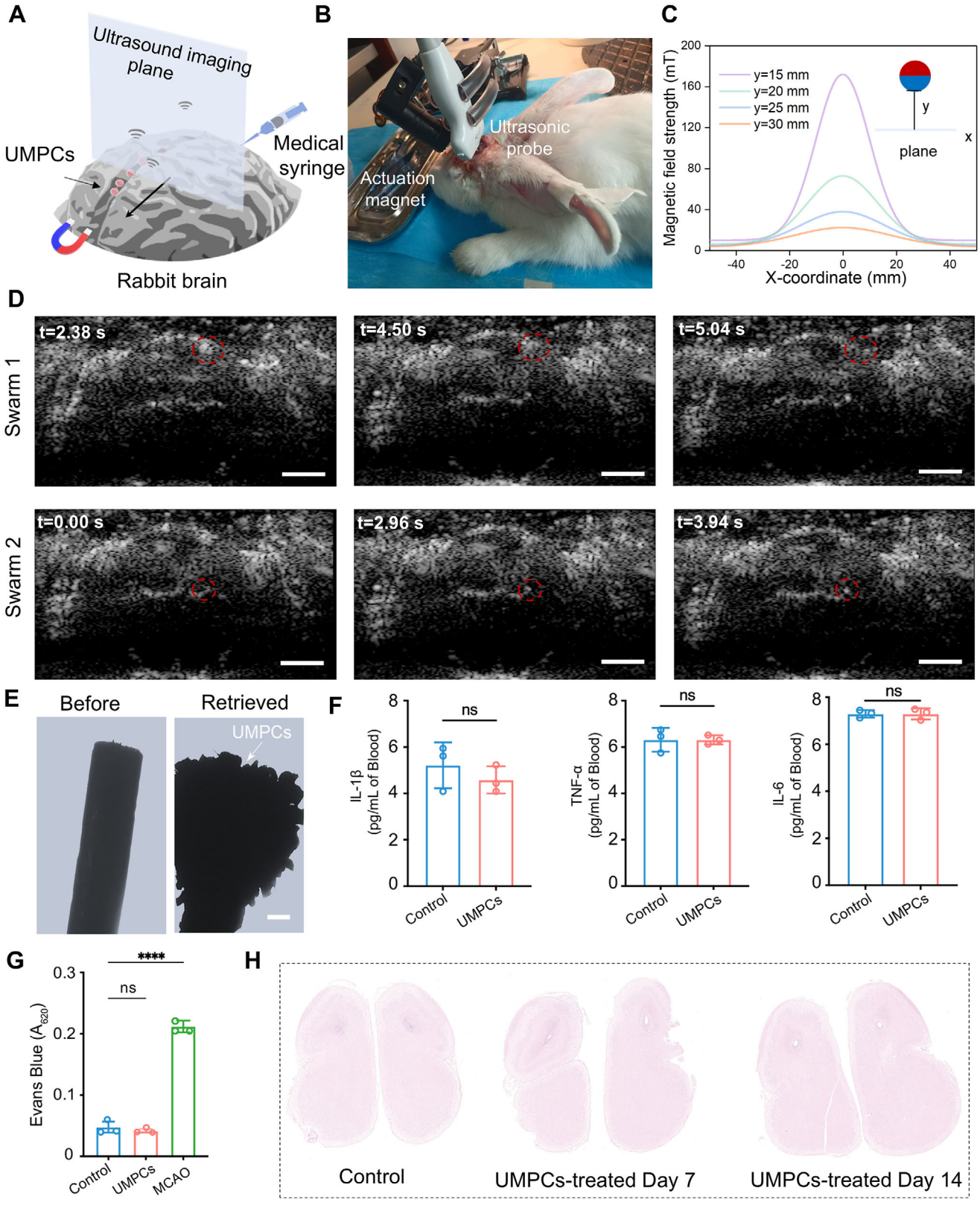

FIGURE 6 | In vivo navigation and biosafety assessment of UMPCs in a rabbit brain. (A,B) Schematic (A) and digital photo (B) of UMPCs injection in CSF under magnetic actuation and being monitored by ultrasound imaging. (C) Intensity distribution of the actuation magnetic field in the xy-plane. (D) Ultrasound images of UMPCs swarm moving in CSF under magnetic manipulation. Scale bar: 5 mm. (E) Optical images of the magnetic needle before and after collecting UMPCs from the CSF. Scale bar: 200 μm. (F) Plasma concentrations of inflammatory cytokines IL-6, TNF-α, and IL-1β. No significant differences were found between control and UMPCs-treated groups ($n = 3$). (G) Absorbance of Evans blue dye at 620 nm for different samples ($n = 3$). (H) Representative images of Prussian blue staining of cerebrum tissues with treatments. Data in (F,G) are presented as the mean ± standard deviation. **** $p < 0.0001$; ns, not significant.

precise control over size and morphology of the microrobot while integrating a porous MOF shell with tailored functional properties. The proposed strategy offers several critical advantages for biomedical applications, particularly in intracranial detoxification. First, the gas-core structure of UMPCs significantly enhances their acoustic reflectivity, making them highly responsive toward ultrafast and super-resolution ultrasound imaging. This enables real-time non-invasive tracking of microrobots in vivo (Figure S45). Second, the PCN-333 (Fe) layer on the surface of UMPCs exhibits strong and selective bilirubin adsorption capacity. The ALD-assisted hydrothermal growth strategy for MOF layer broadens the application scope of UMPCs. Third, the UMPCs exhibit excellent controllability under magnetic field, enabling efficient navigation through complex fluidic environments to perform highly targeted therapeutic tasks. This capability is further reinforced by the remarkable recoverability, significantly mitigating safety concerns associated with potential long-term retention in the human body. Taken together, our study not only pioneers a transformative strategy for targeted toxin clearance in cerebrospinal fluid, but also lays a robust foundation for future clinical translation. Beyond bilirubin clearance, this approach could be adapted for the removal of other harmful metabolites or bioactive molecules. Efficient controlled motion enhances UMPC-target interaction, accelerating molecular capture and enabling precise interventions with high spatial specificity.

Despite these advantages, several challenges and opportunities remain. First, improving the biodegradability or metabolic clearance of UMPCs is essential for future long-term clinical implementation. In this study, UMPCs were retrieved by a magnetic field after removal of the bilirubin. Future work will focus on material optimization to enable spontaneous metabolism and clearance of microrobots by biological systems. Optimizing the internal gas and shell materials of microbubbles is also of great significance for obtaining microrobots with better ultrasound imaging performance. Second, although ultrafast ultrasound imaging successfully tracked the movement of UMPCs in the rabbit brain, challenges remain due to spontaneous diffusion, which leads to decreased population density, and the cerebral blood flow interferes with the quality of ultrasound imaging. Thus, a more efficient and safe integrated imaging system is crucial for real-time visualization, dynamic path planning, and signal feedback. Microrobots will then be combined with a non-invasive and intraoperative imaging system as well as artificial intelligence algorithms to facilitate self-learning imaging in complex internal environments, thereby achieving group manipulation and closed-loop feedback control [48]. Third, the construction of animal models of hyperbilirubinemia will be crucial for therapeutic validation [34, 35]. We plan to establish larger-animal models, such as pigs and sheep, to simulate clinical scenarios more accurately. Conducting detoxification experiments in larger animals helps to obtain more comprehensive and clinically closer experimental data. Finally, a comprehensive evaluation of therapeutic efficacy will integrate histological, immunohistochemical, and chromatographic data with key clinical metrics, including CSF biochemistry and neurological function. This multi-modal evaluation will provide precise insights into the treatment's outcomes, ranging from its biological and molecular effects to clinical impact.

4 | Experimental Section

4.1 | Synthesis of UMPCs

Microbubbles were prepared by microfluidic equipment [49]. Briefly, gas phase, oil phase, and water phase solutions were put into the microfluidic chip in a certain order, and different sizes of gas-containing microbubbles were obtained by adjusting the flow rates of the phases. The microbubbles were solidified by UV light for 30 s, and washed with ethanol and deionized water for three times.

MOF layer was prepared with the assistance of ALD-produced ZnO nanomembranes. In the ALD process, 20 sccm nitrogen was used as carrier gas. Diethyl zinc (diethylzinc, DEZ) was used as zinc source, and deionized water as oxygen source. A typical deposition cycle includes: DEZ pulse (50 ms), waiting time (5 s), N_2 purge (30 s), DI water pulse (30 ms), waiting time (5 s), and N_2 purge (30 s). In the current study, ZnO nanomembrane with certain ALD cycles was deposited on microbubbles. Then, 0.3 g ferric chloride hydrate ($FeCl_3 \cdot 6H_2O$) was dissolved in 50 mL of dimethylformamide (DMF) to prepare solution A. Separately, TATB (0.25 g) was dissolved in 50 mL of DMF to obtain solution B. ALD ZnO nanomembrane-coated microbubbles were then immersed in solution A within a sealed beaker and maintained at 90 °C for 24 h. After cooling to ambient temperature, solution B was introduced. The mixture was resealed and heated to the optimized temperature of 120 °C for an additional 24 h. Subsequently, the sample was rinsed with fresh DMF, and dried at 100 °C for 12 h. This procedure resulted in the deposition of a homogeneous PCN-333 (Fe) layer on the surface of microbubbles. Finally, the microbubbles with PCN-333 (Fe) layer (100 mg) and 1 mL Fe_3O_4 nanoparticles (5 mg/mL) (Jiangsu Xianfeng Nanotechnology Co., Ltd.) were mixed using mechanical stirring for 30 min to prepare UMPCs. The mixture was subjected to magnetic separation, and the collected sample was then dried at 50 °C for 6 h to obtain the final UMPCs.

4.2 | Magnetic Navigation and Ultrasound Imaging Experiments

In the experiments, aCSF was purchased from Qingdao Jieshikang Biotechnology Co., Ltd. In addition, PBS (Solarbio, Cat# P1020), FBS (Solarbio, Cat# S9030), and BSA (Solarbio, Cat# A8010) were also used in the experiments to establish fluidic environments for UMPCs.

Both in vitro and in vivo ultrasound imaging experiments were performed using a commercial multichannel ultrasound platform (Poda-US X10-128, Poda Medical Technology Co., Ltd) and probes centered at 7.8 MHz (pitch = 0.3 mm). A compounded framerate above 1000 Hz was achieved by ultrafast B-mode imaging and ultrafast Doppler imaging based on coherent multi-angle plane-wave ultrasound transmissions (5 steering angles, pulse-repetition-frequency (PRF) >= 5000 Hz), which contributed to the real-time monitoring during the navigation of UMPCs. Post-processing of radio-frequency (RF) signals was operated offline due to the high framerate. Imaging reconstruction was accomplished by a customized GPU-based delay-and-sum beam-

former, reaching the efficiency of approximately 5000 frames·s^{-1} with GeForce RTX 3060 (Table S1). Before Doppler imaging, a singular value decomposition (SVD) spatial-temporal filter was utilized to separate moving UMPCs from the static background. All data were processed using Matlab (Mathworks, Natick, VA, USA).

4.3 | Bilirubin Removal Experiments

To evaluate the adsorption kinetics of bilirubin by UMPCs, 50 mg of the sample was added to 5 mL of a bilirubin/PBS solution (120 mg·L^{-1}) to initiate the adsorption process. The absorbance of the solution at 438 nm was measured at specified time intervals. The bilirubin uptake at time t(q_t) was calculated using the following formula:

$$q_t = (C_0 - C_t) \times V/m \quad (1)$$

where q_t (mg·g^{-1}) is the mass of bilirubin adsorbed per unit mass of MOF at t time; C_0 (mg·L^{-1}) and C_t (mg·L^{-1}) are the initial bilirubin concentration and residual bilirubin concentration at t time respectively; V (mL) is the solution volume; m (g) is the mass of UMPCs. For the adsorption kinetic model, see Table S3.

In order to evaluate the adsorption isotherm of bilirubin by UMPCs, 100 mg UMPCs was added to 5 mL bilirubin/PBS solution with the initial concentration of 300, 350, 400, 700, 800, 900, and 1000 mg·L^{-1}, and the absorbance was measured and calculated by the following formula:

$$q_e = (C_0 - C_e) \times V/m \quad (2)$$

In order to evaluate the adsorption of bilirubin by UMPCs in high protein environment, the bilirubin/BSA solution with 150 mg·L^{-1} bilirubin and 40 mg·mL^{-1} (40 000 mg·L^{-1}) BSA was prepared, and 20 mg UMPCs was added to 5 mL bilirubin/BSA solution. The absorbance of the supernatant at different times was measured and the adsorption efficiency was calculated. The above experiments were carried out in dark to prevent the decomposition of bilirubin by light.

4.4 | In Vitro Experiments

The gelatin brain phantom was placed in a 3D printed cranial mold, and then 10 mL 30 mg·L^{-1} bilirubin solution and 100 mg UMPCs were added into the gap between the phantom and the cranial. The magnetic actuation of UMPCs was then monitored by the ultrafast ultrasound imaging probe, and the concentration of bilirubin in the channel was measured and compared with the control group.

4.5 | In Vivo Experiments

All animal experiments were approved by the Animal Research Ethics Committee, Fudan University (202202020Z). Three-month-old New Zealand rabbits were used in the experiments. Anesthesia was induced and maintained with Zoletil 50. The rabbit underwent surgical craniotomy before real-time ultrasound monitoring so as to accomplishing UMPCs injections and improving ultrasound imaging quality as well. A sagittal skin incision was performed across the posterior part of the head. The entire width of the skull was exposed by removing both the skin and the periosteum using fine straight scissors. After determining the size of cranial window estimated by the ultrasonic probe, the parietal bone was removed by drilling a rectangular flap and gently moving the bone away from the dura mater. An indwelling needle was used to place a catheter between the arachnoid and the pia mater, and UMPCs were then injected into the subarachnoid space. Subsequently, UMPCs moving in CSF driven by a magnet were real-time monitored under ultrafast ultrasound imaging. NdFeB magnetic needle (r = 0.5 mm) coated with a 10 nm Ti layer was used to retrieve UMPCs from CSF after the treatment. After disinfection, the wound was sutured, and the New Zealand rabbits were fed for long time. Longitudinal measurements of rabbit body weight were obtained at predetermined time points. For histological analysis, the rabbits were euthanized, the tissues of heart, brain, liver, kidney, spleen, and lung were extracted and stained, and the organ and tissue sections were obtained and compared with those of normal rabbits and craniotomy-treated rabbits. Cerebrum tissue sections from different experimental groups were subjected to Prussian blue staining according to standard protocols to detect the deposition of iron. The level of oxidative stress was also assessed by measuring key biomarkers including MDA and SOD, quantified using assay kits (Beyotime Corp, China, S0131S and S0101S). Besides, blood samples were collected, and plasma was separated by centrifugation. The concentrations of specific inflammatory cytokines were measured using a standard enzyme-linked immunosorbent assay (ELISA) kit. BBB integrity was also evaluated by Evans blue dye extravasation. MCAO model was included to induce definitive BBB disruption and served as a positive control. After the procedure, dye was then extracted from cerebral tissues, and its concentration was quantified by measuring absorbance at 620 nm.

4.6 | Strain Simulation

We adopted the finite element analysis method to simulate the stress distribution and deformation of microbubbles when subjected to local loads. First, we selected a 3D space as the basis of the initial model. As shown in Figure 2b, we established six spherical models with different shell thickness-to-core radius ratios. A fixed constraint was set on a very small circular surface at the bottom of the microbubble to ensure that the microbubble would not move. Then, a pressure load of 1 MPa was applied to the microbubble along the z direction with an area of approximately 18.7 μm^2 at the top of the microbubble, and a free domain was added to the microbubble to enable it to deform freely. The deformation strain of the microbubbles was then simulated. For global compression pressure applied, a parametric sweep analysis was performed to determine the stress evolution within the shell, and the volume compression ratios were also calculated to evaluate the influence from the external pressure.

4.7 | Statistical Analysis

The statistical analysis and visualization were performed with GraphPad Prism 9.3.1. All experimental data were expressed as mean and standard deviation. Comparisons between two groups were analyzed by student's t test, while data were assessed using one-way analysis of variance (ANOVA). For repeated measurements of the same group of samples across multiple time points, repeated measures ANOVA was applied. p value < 0.05 was considered as statistically significant. Asterisks indicate significant differences (****$p < 0.0001$ and ***$p < 0.001$).

Acknowledgements

This work was supported by National Key Technologies R&D Program of China (2021YFA0715302), National Natural Science Foundation of China (Nos. 525B1002, 62375054, 52203328, 52473254, 12274093 and 523B2107), Science and Technology Commission of Shanghai Municipality (Nos. 24520750200, 24CL2900200 and 23490713500), and Shanghai Talent Programs. Part of the experimental work was carried out in Fudan Nanofabrication Laboratory. The authors would like to thank Ceshihui (www.Ceshihui.com) for their help with the XRD and the Micro-and Nanofabrication Lab at Yiwu Research Institute for their technical support.

Funding

National Key Technologies R&D Program of China (2021YFA0715302), National Natural Science Foundation of China (525B1002, 62375054, 52203328, 52473254, 12274093 and 523B2107), and Science and Technology Commission of Shanghai Municipality (24520750200, 24CL2900200 and 23490713500).

Conflicts of Interest

The authors declare no conflicts of interest.

Data Availability Statement

The data that support the findings of this study are available from the corresponding author upon reasonable request.

References

1. F. W. Vonberg, A. Dawson, G. Scott, and N. Davies, "Aciclovir-induced Neurotoxicity," *Practical Neurology* 23 (2023): 157–159.

2. M. Assem, M. Lando, M. Grissi, et al., "The Impact of Uremic Toxins on Cerebrovascular and Cognitive Disorders," *Toxins* 10 (2018): 303.

3. N. Alperin and R. Burman, "A Mechanism Linking Sleep with CSF-to-Blood Toxins Clearance," *Alzheimer's & Dementia* 20 (2024): 085021.

4. R. Burman and N. Alperin, "CSF-to-blood Toxins Clearance Is Modulated by Breathing through Cranio–spinal CSF Oscillation," *Journal of Sleep Research* 33 (2024): 14029.

5. K. Kjellin, "Bilirubin Compounds in the CSF," *Journal of the Neurological Sciences* 13 (1971): 161–173.

6. V. Klose, S. Jesse, J. Lewerenz, et al., "Blood–CSF Barrier Integrity in Amyotrophic Lateral Sclerosis," *Brain* 147 (2024): 4254–4264.

7. M. M. Sarabi, E. Babaeenezhad, M. Amini, M. Kaviani, and F. Naghibalhossaini, "Bilirubin and Epigenetic Modifications in Metabolic and Immunometabolic Disorders," *Endocrine, Metabolic & Immune Disorders-Drug Targets* 22 (2022): 1178–1190.

8. A. Qureshi and N. Akhtar, "Bilirubin Inclusions in Neonatal Neutrophils. *Blood*," *The Journal of the American Society of Hematology* 130 (2017): 1601–1601.

9. C. Mancuso, "Bilirubin and Brain: a Pharmacological Approach," *Neuropharmacology* 118 (2017): 113–123.

10. K. Lai, X. Song, H. Shi, et al., "Bilirubin Enhances the Activity of ASIC Channels to Exacerbate Neurotoxicity in Neonatal Hyperbilirubinemia in Mice," *Science Translational Medicine* 12 (2020): aax1337.

11. R. Fujiwara, M. Haag, E. Schaeffeler, A. T. Nies, U. M. Zanger, and M. Schwab, "Systemic Regulation of Bilirubin Homeostasis: Potential Benefits of Hyperbilirubinemia," *Hepatology* 67 (2018): 1609–1619.

12. H. Yang, L. Wang, and X. Huang, "MOF-based Micro/Nanomotors (MOFtors): Recent Progress and Challenges," *Coordination Chemistry Reviews* 495 (2023): 215372.

13. X. Wang, X. Chen, C. C. J. Alcântara, et al., "MOFBOTS: Metal–organic-framework-based Biomedical Microrobots," *Advanced Materials* 31 (2019): 1901592.

14. A. Terzopoulou, M. Palacios-Corella, C. Franco, et al., "Biotemplating of Metal–organic Framework Nanocrystals for Applications in Small-scale Robotics," *Advanced Functional Materials* 32 (2022): 2107421.

15. Q. Li, W. Zhao, H. Guo, et al., "Metal–organic Framework Traps with Record-high Bilirubin Removal Capacity for Hemoperfusion Therapy," *ACS Applied Materials & Interfaces* 12 (2020): 25546–25556.

16. S. Wu, P. Yue, Y. Ma, Y. Zou, W. Liang, and Q. Ye, "Hemoperfusion Adsorbents for Removal of Common Toxins in Liver and Kidney Failure: Recent Progress, Challenges, and Prospects," *Advanced Materials* 37 (2023): 2305152.

17. J. Sun, R. Chu, X. Wu, et al., "Anti-biopassivated Reticular Micromotors for Bladder Cancer Therapy," *Journal of the American Chemical Society* 147 (2025): 17936–17945.

18. H. Han, X. Ma, W. Deng, et al., "Imaging-guided Bioresorbable Acoustic Hydrogel Microrobots," *Science Robotics* 9 (2024): adp3593.

19. Y. Dong, L. Wang, Z. Zhang, et al., *Science Advances* 40 (2022): abq8573.

20. B. J. Nelson and S. Pané, "Delivering Drugs with Microrobots," *Science* 382 (2023): 1120–1122.

21. J. Li, B. Esteban-Fernández de Ávila, W. Gao, L. Zhang, and J. Wang, "Micro/Nanorobots for Biomedicine: Delivery, Surgery, Sensing, and Detoxification," *Science robotics* 2 (2017): aam6431.

22. Z. Wu, L. Li, Y. Yang, et al., "A Microrobotic System Guided by Photoacoustic Computed Tomography for Targeted Navigation in Intestines in Vivo," *Science Robotics* 4 (2019): aax0613.

23. B. E. de Ávila, P. Angsantikul, J. Li, et al., "Micromotor-enabled Active Drug Delivery for in Vivo Treatment of Stomach Infection," *Nature Communications* 8 (2017): 272.

24. F. Zhang, Z. Li, Y. Duan, et al., "Gastrointestinal Tract Drug Delivery Using Algae Motors Embedded in a Degradable Capsule," *Science Robotics* 7 (2022): abo4160.

25. J. Yoo, S. Tang, and W. Gao, "Micro-and Nanorobots for Biomedical Applications in the Brain," *Nature Reviews Bioengineering* 1 (2023): 308–310.

26. R. Nauber, S. R. Goudu, M. Goeckenjan, M. Bornhäuser, C. Ribeiro, and M. Medina-Sánchez, "Medical Microrobots in Reproductive Medicine from the Bench to the Clinic," *Nature Communications* 14 (2023): 728.

27. H. Zhang, Z. Li, C. Gao, et al., "Dual-responsive Biohybrid Neutrobots for Active Target Delivery," *Science Robotics* 6 (2021): aaz9519.

28. S. Tang, F. Zhang, H. Gong, et al., "Enzyme-powered Janus Platelet Cell Robots for Active and Targeted Drug Delivery," *Science Robotics* 5 (2020): aba6137.

29. S. Tang, D. Tang, H. Zhou, et al., "Bacterial Outer Membrane Vesicle Nanorobot," *Proceedings of the National Academy of Sciences* 121 (2024): 2403460121.

30. Z. Wu, T. Li, W. Gao, et al., "Cell-membrane-coated Synthetic Nanomotors for Effective Biodetoxification," *Advanced Functional Materials* 25 (2015): 3881–3887.

31. C. J. Hu, R. H. Fang, J. Copp, B. T. Luk, and L. Zhang, "A Biomimetic Nanosponge That Absorbs Pore-forming Toxins," *Nature Nanotechnology* 8 (2013): 336–340.

32. B. E. de Ávila, P. Angsantikul, D. E. Ramirez-Herrera, et al., "Hybrid Biomembrane–functionalized Nanorobots for Concurrent Removal of Pathogenic Bacteria and Toxins," *Science Robotics* 3 (2018): aat0485.

33. H. Chen, H. Zhu, Y. Wang, et al., "Structural Coloration by Internal Reflection and Interference in Hydrogel Microbubbles and Their Precursors," *Advanced Optical Materials* 9 (2021): 2100259.

34. J. Wang, Y. Jiang, F. Zhu, et al., "Design and Assembly of Continuous Macro-micro-porous Metal-organic Framework Film Assisted by Atomic Layer Deposition for Biosensing," *Advanced Functional Materials* 35 (2025): 2419775.

35. J. Wang, J. Tan, Z. Zhao, et al., "Controllable Ion Design in Flexible Metal Organic Framework Film for Performance Regulation of Electrochemical Biosensing," *Biosensors and Bioelectronics* 260 (2024): 116433.

36. Z. Zhao, Y. Kong, G. Huang, et al., "Area-selective and Precise Assembly of Metal Organic Framework Particles by Atomic Layer Deposition Induction and Its Application for Ultra-sensitive Dopamine Sensor," *Nano Today* 42 (2022): 101347.

37. Z. Zhao, X. Ke, J. Huang, et al., "Design and Synthesis of Transferrable Macro-sized Continuous Free-standing Metal-organic Framework Films for Biosensor Device," *Advanced Science* 11 (2024): 2310189.

38. G. Qiao, D. Guan, S. Yuan, et al., "Perovskite Quantum Dots Encapsulated in a Mesoporous Metal–organic Framework as Synergistic Photocathode Materials," *Journal of the American Chemical Society* 143 (2021): 14253–14260.

39. M. Qiao, Y. Li, Y. Li, M. Chang, X. Zhang, and S. Yuan, "Unlocking of Hidden Mesopores for Enzyme Encapsulation by Dynamic Linkers in Stable Metal-organic Frameworks," *Angewandte Chemie International Edition* 63 (2024): 202409951.

40. M. Sun, K. F. Chan, Z. Zhang, et al., "Magnetic Microswarm and Fluoroscopy-guided Platform for Biofilm Eradication in Biliary Stents," *Advanced Materials* 34 (2022): 2201888.

41. W. Sun, J. Hou, Y. Zhou, et al., "Amorphous FeSnOx Nanosheets with Hierarchical Vacancies for Room-temperature Sodium-sulfur Batteries," *Angewandte Chemie, International Edition* 63 (2024): 202404816.

42. B. Wang, J. Shen, C. Huang, et al., "Magnetically Driven Biohybrid Blood Hydrogel Fibres for Personalized Intracranial Tumour Therapy under Fluoroscopic Tracking," *Nature Biomedical Engineering* 9 (2025): 1471–1485.

43. S. Cheng, J. Zou, S. Yan, et al., "Vascular Ultrasound Imaging with Flexible Wearable Array," *Measurement Science and Technology* 36 (2025): 055404.

44. Y. Yuan, Y. Yang, X. Ma, et al., "Molecularly Imprinted Porous Aromatic Frameworks and Their Composite Components for Selective Extraction of Uranium Ions," *Advanced Materials* 30 (2018): 1706507.

45. Y. Liu, Z. Wang, C. Liu, et al., "Supramolecular Organic Frameworks as Adsorbents for Efficient Removal of Excess Bilirubin in Hemoperfusion," *ACS Applied Materials & Interfaces* 14 (2022): 47397–47408.

46. B. Li, X. Zhang, J. Shen, A. Zhang, and H. Huang, "Bimetallic PCN-333 with Modulated Crystallization and a Porosity Structure for a Highly Efficient Removal of congo Red," *ACS Omega* 9 (2024): 7173–7187.

47. S. Wu, P. Yue, Y. Ma, Y. Zou, W. Liang, and Q. Ye, "Hemoperfusion Adsorbents for Removal of Common Toxins in Liver and Kidney Failure: Recent Progress, Challenges, and Prospects," *Advanced Materials* 37 (2023): 2305152.

48. M. Medany, S. K. Mukkavilli, and D. Ahmed, "AI-driven Autonomous Microrobots for Targeted Medicine," *Nature Reviews Bioengineering* 2 (2024): 914–915.

49. X. Lin, H. Zhu, Z. Zhao, et al., "Hydrogel-based Janus Micromotors Capped with Functional Nanoparticles for Environmental Applications," *Advanced Materials Technologies* 5 (2020): 2000279.

Supporting Information

Additional supporting information can be found online in the Supporting Information section.

Supporting File 1: adma71880-sup-0001-SuppMat.pdf
Supporting File 2: adma71880-sup-0002-VideoS1.mp4
Supporting File 3: adma71880-sup-0003-VideoS2.mp4
Supporting File 4: adma71880-sup-0004-VideoS3.mp4
Supporting File 5: adma71880-sup-0005-VideoS4.mp4
Supporting File 6: adma71880-sup-0006-VideoS5.mp4
Supporting File 7: adma71880-sup-0007-VideoS6.mp4